



Article

Potential Novel Thioether-Amide or Guanidine-Linker Class of SARS-CoV-2 Virus RNA-Dependent RNA Polymerase Inhibitors Identified by High-Throughput Virtual Screening Coupled to Free-Energy Calculations

Marko Jukič^{1,2} , Dušanka Janežič^{2,*} and Urban Bren^{1,2,*}

¹ Laboratory of Physical Chemistry and Chemical Thermodynamics, Faculty of Chemistry and Chemical Engineering, University of Maribor, Smetanova 17, SI-2000 Maribor, Slovenia; marko.jukic@um.si

² Faculty of Mathematics, Natural Sciences and Information Technologies, University of Primorska, Glagoljaška 8, SI-6000 Koper, Slovenia

* Correspondence: dusanka.janezic@upr.si (D.J.); urban.bren@um.si (U.B.)

Abstract: SARS-CoV-2, or severe acute respiratory syndrome coronavirus 2, represents a new pathogen from the family of *Coronaviridae* that caused a global pandemic of COVID-19 disease. In the absence of effective antiviral drugs, research of novel therapeutic targets such as SARS-CoV-2 RNA-dependent RNA polymerase (RdRp) becomes essential. This viral protein is without a human counterpart and thus represents a unique prospective drug target. However, in vitro biological evaluation testing on RdRp remains difficult and is not widely available. Therefore, we prepared a database of commercial small-molecule compounds and performed an in silico high-throughput virtual screening on the active site of the SARS-CoV-2 RdRp using ensemble docking. We identified a novel thioether-amide or guanidine-linker class of potential RdRp inhibitors and calculated favorable binding free energies of representative hits by molecular dynamics simulations coupled with Linear Interaction Energy calculations. This innovative procedure maximized the respective phase-space sampling and yielded non-covalent inhibitors representing small optimizable molecules that are synthetically readily accessible, commercially available as well as suitable for further biological evaluation and mode of action studies.

Keywords: COVID-19; SARS-CoV-2 virus; RNA-dependent RNA polymerase; binding site identification; virtual screening; non-covalent inhibitors; in silico drug design; molecular dynamics; free-energy calculations; ensemble docking



Citation: Jukič, M.; Janežič, D.; Bren, U. Potential Novel Thioether-Amide or Guanidine-Linker Class of SARS-CoV-2 Virus RNA-Dependent RNA Polymerase Inhibitors Identified by High-Throughput Virtual Screening Coupled to Free-Energy Calculations. *Int. J. Mol. Sci.* **2021**, *22*, 11143. <https://doi.org/10.3390/ijms222011143>

Academic Editor: Gerard Pujadas

Received: 21 September 2021

Accepted: 13 October 2021

Published: 15 October 2021

Publisher's Note: MDPI stays neutral with regard to jurisdictional claims in published maps and institutional affiliations.



Copyright: © 2021 by the authors. Licensee MDPI, Basel, Switzerland. This article is an open access article distributed under the terms and conditions of the Creative Commons Attribution (CC BY) license (<https://creativecommons.org/licenses/by/4.0/>).

1. Introduction

In late 2019–early 2020, scientific and medicinal communities identified a novel human pathogen—severe acute respiratory syndrome coronavirus 2 (SARS-CoV-2) causing a pandemic named COVID-19 [1]. This pathogen belongs to the *Coronaviridae* family and represents a positive-sense single-stranded RNA (+ssRNA) virus [2,3]. Previous occurrences of related pathogens can be traced to 2003 when coronaviruses were reported to cause severe acute (SARS) and Middle East (MERS) respiratory syndromes [4–6]. The COVID-19 disease is of grave global concern because, while the majority of cases display mild symptoms, a variable percentage (0.2 to >5%) of patients progress to pneumonia and multi-organ failure leading to potential death, especially without medical assistance [7–12].

At the time, there were no registered drugs against SARS-CoV-2, and only several drug repurposing strategies have been reported [13–24]. Current therapeutic options include direct-acting remdesivir, symptomatic treatment or immunomodulatory approaches mainly targeting host responses (dexamethasone, tocilizumab, sarilumab mitigating IL-6 response) [25–28]. Many clinical studies are ongoing, albeit also with disadvantageous re-

sults such as the recent retractions of chloroquine and hydroxychloroquine drugs suggested for the treatment of COVID-19 [29].

In the context of only a handful of therapeutic options to fight this global threat, we performed a novel drug design and virtual screening study in order to identify potential inhibitors of the RNA-dependent RNA polymerase (RdRp) of SARS-CoV-2. RdRp catalyzes the synthesis of an RNA strand complementary to a given RNA template [30,31]. This essential viral enzyme is highly conserved among (+ssRNA) viral species and, as such, devoid of a human counterpart promoting this protein to a viable, under-investigated and prospective therapeutic target [32,33]. Moreover, the complexity of RNA replication machinery involving a synchronized action of multiple viral and host proteins towards final RNA polymerization makes this target a difficult system for designing *in vitro* biological experiments [34,35]. Furthermore, current postulated activities on RdRp rely on (infected) whole cell-line experimental data and on conducted preclinical *in vivo* data, further emphasizing the need for a thorough *in silico* computer-assisted drug design approach [36,37].

The RdRp forms a part of the Replicase polyprotein 1ab (Uniprot P0DTD1, sequence location 4393–5324; nsp12). Based on the cryoEM structure of the SARS-CoV reported by Kirchdorfer et al., RdRp contains a polymerase domain described in the literature as “right hand” (PDB ID: 6NUR numbering; 398–919) similar to other polymerases [38]. The domain itself consists of fingers (398–581, 628–687), palm (582–627, 688–815) and thumb (816–919) subdomains (Figure 1). The palm subdomain, composed of a four-stranded antiparallel beta sheet and two alpha helices, represents the most conserved structural motif. The SARS-CoV nsp12 also contains two structural Zn binding sites, both distal to the active site and not involved in any protein–protein or protein–RNA interactions. While the outer surface of the protein is predominantly negatively charged, the RNA binding groove carries a net positive charge. The active site of RdRps is in general highly conserved and includes two successive aspartate residues protruding from a beta-turn at the nucleotide channel of the palm subdomain [39,40].

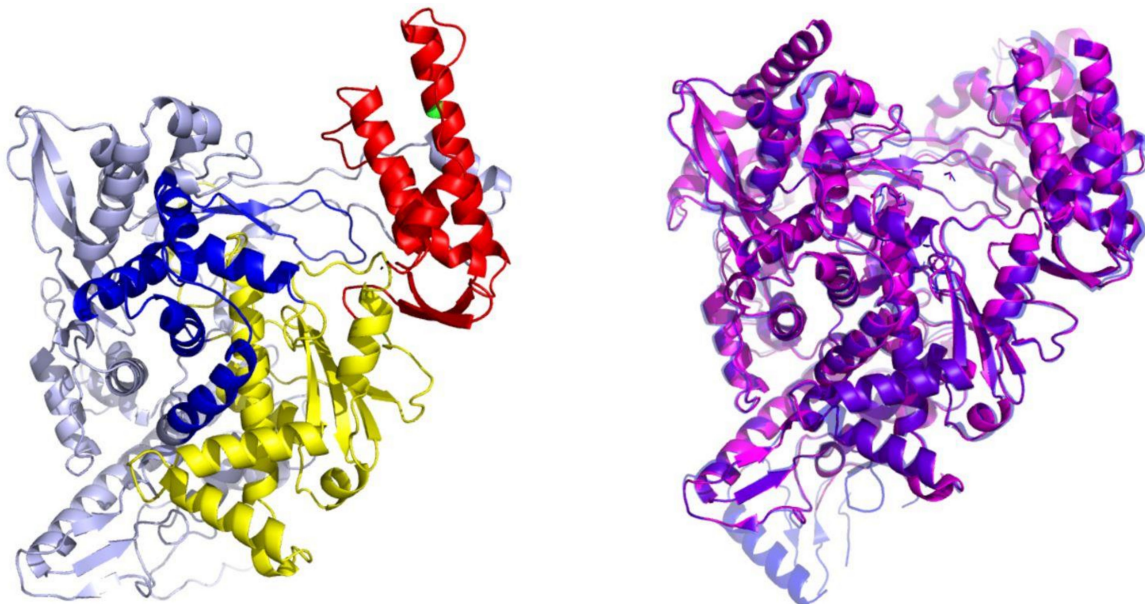


Figure 1. (Left) Structure of a typical viral RdRp. The protein is presented in a cartoon model with thumb subdomain colored in red, palm subdomain in yellow and fingers subdomain in blue. The RNA channel groove is located in the central cavity encircled by all three subdomains. (Right) Superimposition of the SARS-CoV (PDB ID: 6NUR, magenta colored cartoon model) and the recently published cryoEM of SARS-CoV-2 RdRp (PDB ID: 6M71, blue colored cartoon model) revealing a virtually identical structural architecture.

The SARS-CoV (PDB ID: 6NUR, nsp12, chain A) and SARS-CoV-2 (P0DTD1, RdRp) RdRp amino-acid sequences are 94% similar as calculated by the Clustal software (identical positions 897, similar positions 30, identity: 93.9%) [41]. Moreover, examining the recently reported cryoEM structures of SARS-CoV-2 RdRp by Gao et al. (PDB ID: 6M71 and 7B3D), the structural conservation to SARS-CoV RdRp (all atom RMSD of 0.6 Å) can be clearly observed as well (Figure 1) [42,43]. The binding mode of RdRp is described by Yin et al. (PDB ID: 7BV2) [44].

RdRp has been already targeted in different RNA viruses, including Hepatitis C Virus (HCV), Norovirus, Zika Virus (ZIKV), and coronaviruses (CoVs) [45–48]. Nevertheless, only a single drug, sofosbuvir, is registered with HCV indication (RdRp pharmacodynamics), and a handful of nucleoside and non-nucleoside inhibitors are under investigation as reviewed by Powrill et al. (Figure 2) [49]. The binding modes of developed inhibitors are elaborated in the literature [50,51]. Moreover, remdesivir, a prodrug currently authorized for emergency use for the SARS-CoV-2 treatment, shares its pharmacophoric traits with the registered drug sofosbuvir and represents a prime example of a viral nucleoside RdRp inhibitor [52–54].

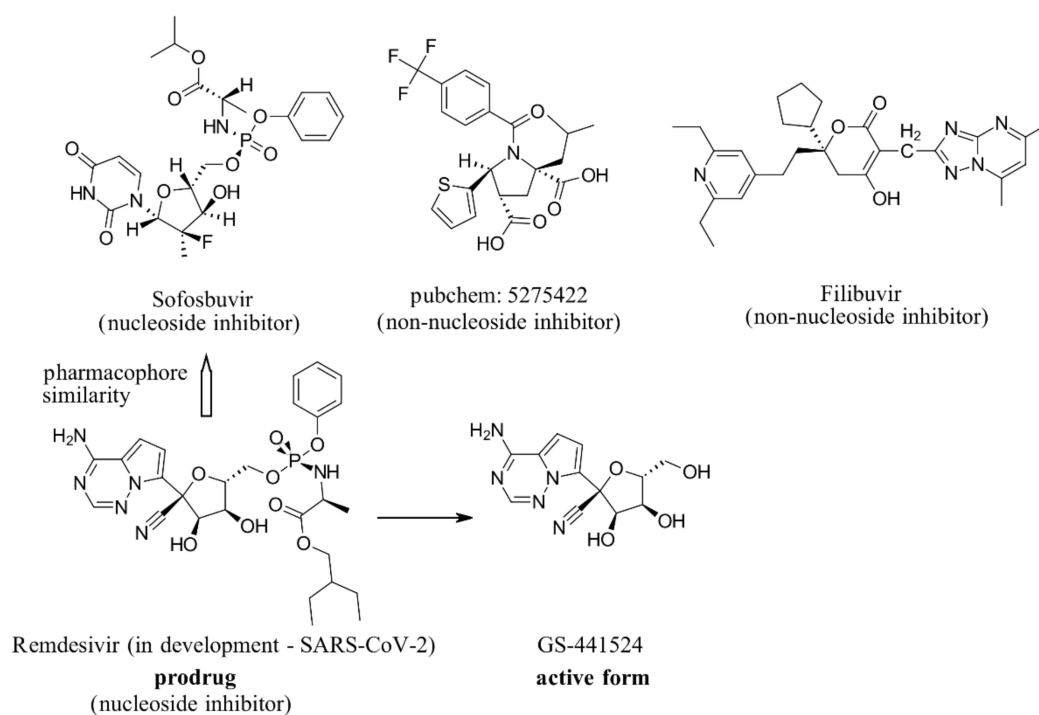


Figure 2. Some of the existing nucleoside and non-nucleoside inhibitors of RdRps found in the scientific literature primarily developed against HCV.

Viability of RdRp as a drug target has been extensively studied beforehand *in silico* by Aftab et al. [55]. We firmly believe the SARS-CoV-2 RdRp represents a validated and underexplored target, supported by experimental data for the development of potential anti COVID-19 drugs, especially in the field of non-covalent, non-nucleoside RNA-dependent RNA polymerase small-molecule inhibitors (Figure 2).

2. Database Preparation

We started preparing an in-house contemporary *in silico* database suitable for VS (virtual screening) or HTVS (high-throughput virtual screening) applications. This database is by its design tailored towards drug-like, small-molecule selection of synthetically accessible and commercially available compounds that should also facilitate fast analogue collection or preparation as well as efficient CPU-time in downstream calculations (Figure 3).

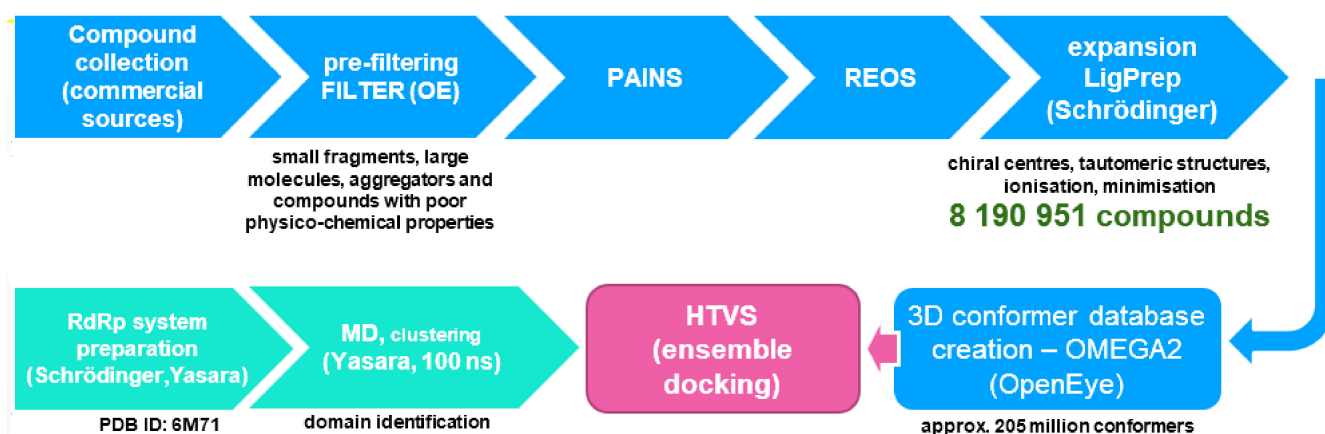


Figure 3. Database preparation for the subsequent high-throughput virtual screening (HTVS) on the SARS-CoV-2 RNA-dependent RNA polymerase (RdRp, PDB ID: 6M71). The final database before conformer generation contained 8 190 951 molecules.

We combined various commercial compound sources (e.g., ENAMINE, Vitas-M, Chembridge, Maybridge, Ambinter, Otava, PrincetonBIO, Key-Organics, Life Chemicals, Uorsy, Specs) and pre-filtered all compounds in order to exclude small fragments or extra-large molecules, aggregators, and compounds with poor physico-chemical properties. This step was performed using OpenEye FILTER software (OpenEye Scientific Software, Inc., Santa Fe, NM, USA) and the following parameters: min_molwt 250, max_molwt 800, min_solubility moderately, eliminate known and predicted aggregators and allowed elements: H, C, N, O, F, S, Cl, Br, I, P. The obtained database was subsequently filtered for *pains* (pan-assay interference compounds) [56,57] and *reos* (rapid elimination of swill) structures in order to eliminate reactive and labile functional groups. Therefore, Knime software with RDKit software nodes was applied to compare all structures in the library to the selection of SMARTS-formatted flags and to remove hits from the database [58].

We ended up with a collection of approximately 4 million compounds that were expanded in the subsequent step where final enumeration of undefined chiral centers, tautomeric structures, removal of structural faults, ionization at the pH of 7.4 and minimization (using OPLS3 force-field) towards the final 3D conformation was performed [59]. For this step, the Ligprep tool by Schrödinger (Release 2021-1, Schrödinger, LLC, New York, NY, USA, 2021) was employed [60,61]. The final database thus consisted of 8 190 951 molecules and was ultimately used for conformer 3D-database preparation with the OpenEye OMEGA2 tool (OpenEye Scientific Software, Inc., Santa Fe, NM, USA). The maximum number of conformations was set at 25 and RMSD threshold of 0.8 Å afforded 205 million compound conformations ready for HTVS.

3. Molecular Dynamics and Clustering

The available Cryo-electron microscopy SARS-CoV-2 RNA-dependent RNA polymerase in complex (four protein chains, 1122 residues, 17800 atoms) with cofactors (PDB ID: 6M71; Resolution: 2.90 Å; by Gao et al. [42,62]) was prepared with Yasara (19.6.6.L.64) software [63]. Missing hydrogens were added, overlapping atoms adjusted, missing residues and atoms incorporated, hydrogen bonds optimized, proteins capped (Ace-4 positions, Nma-4 positions) and residue ionization assigned at pH = 7.4 [64,65]. A cubic box (10 Å away from all atoms) was solvated using TIP3P water model (81749 water molecules) and 0.9% of NaCl (234 Na⁺ and 226 Cl⁻ ions) to achieve physiological ionic power and electroneutrality. After removing bumps/clashes with a steepest descent minimization, an annealing minimization was used to reach a stable local energy minimum. From there, the molecular dynamics (MD) simulation was started by assigning random initial velocities and slowly heating the system up to 298 K. A 100 ns simulation using an AMBER14 force field for the solute, GAFF and AM1BCC charges for the ligands as well as TIP3P water was

initiated (total number of atoms: 263,547). The equations of motion were integrated with a multiple timestep of 1.25 fs for bonded interactions and 2.5 fs for non-bonded interactions at a temperature of 298 K and a pressure of 1 atm (NPT ensemble, Berendsen baro- and thermostat, coupling to the time average temperature and density) with snapshots saved every 100 ps [63,66]. Long-range electrostatic interactions were calculated with the Particle Mesh Ewald algorithm [67]. The SHAKE algorithm was not applied in the simulation. Energy parameters of the system were stable throughout the production run as was the root-mean-square deviation (RMSD) of the protein backbone. No major conformation changes and chain movements were observed during the production run. MD snapshots in 100 ps intervals were collected, and the 1000 obtained protein conformations were aligned onto the starting snapshot followed by the structural clustering using ClusCo software [68]. Its parameters used were hierarchical clustering in a pairwise average-linkage manner with a backbone RMSD score (Figure 4). Twenty clusters were obtained by the ClusCo, and their centroid structures were considered as protein conformations that represent the flexibility of the SARS-Cov-2 RdRp and were used for ensemble docking in the subsequent step (Figure 4, right).

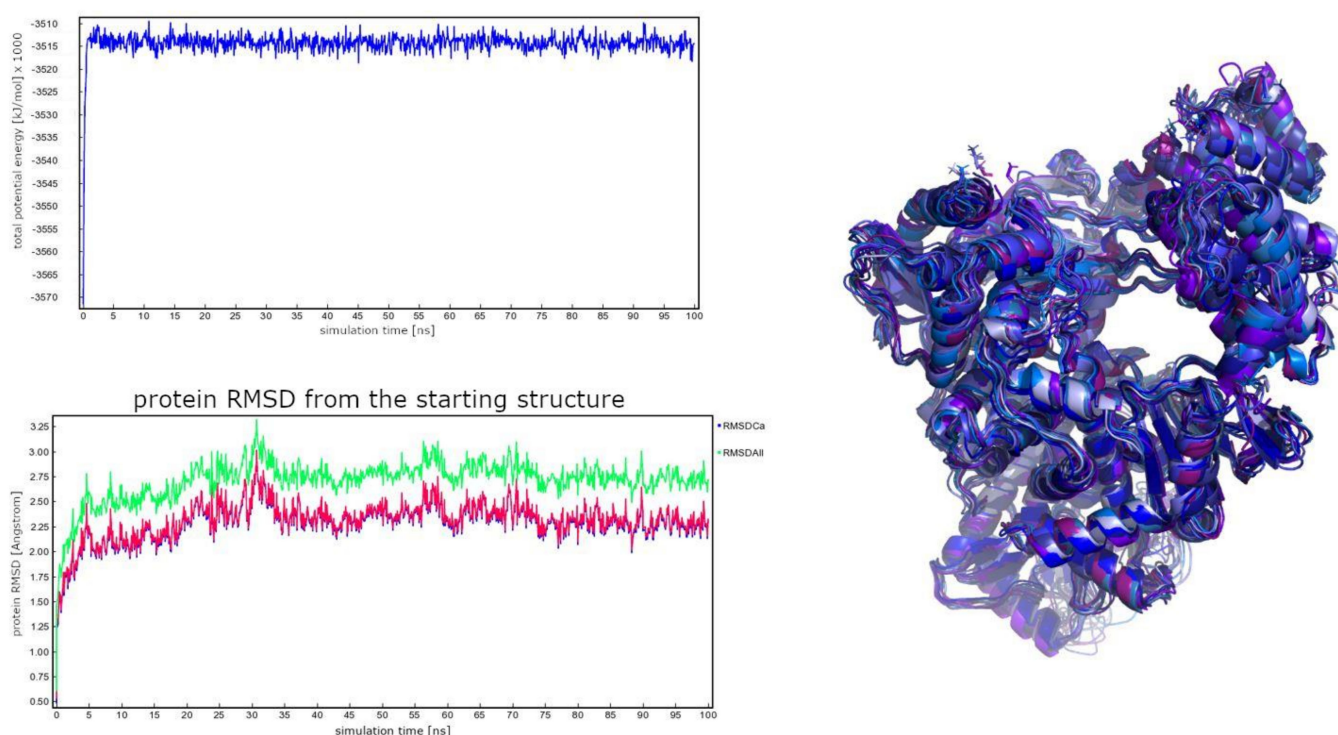


Figure 4. (Left) total potential energy of the system and protein RMSD during the 100 ns MD trajectory (red line depicts CA atoms and green line all atoms). (Right) Superimposition of cluster centroids obtained using the ClusCo software representing the observed conformational flexibility of the SARS-CoV-2 RdRp.

4. Target Preparation

Initial structure alignment and domain identification was performed using NCBI NC_045512 sequence and InterPro, PsiPred and CATH servers [69–71]. After structure preparation, we used superimposition of HCV RdRp in complex with sofosbuvir (2'-deoxy-2'-fluoro-2'-methyluridine-5'-(trihydrogen diphosphate) small molecule RdRp inhibitor) published by Appleby, TC et al. (PDB ID: 4WTG) performed by Open Source PyMOL, release 2.1 and Schrödinger Small-Molecule Discovery Suite (Schrödinger LLC, New York, NY, USA) [72]. Sofosbuvir was positioned analogously to the remdesivir postulated by Gao et al. (Figure 5) [42]. The binding site was thus located above the palm and between the finger/thumb subdomains around our reference small-molecule ligand sofosbuvir as described below (Figure 5) [73].

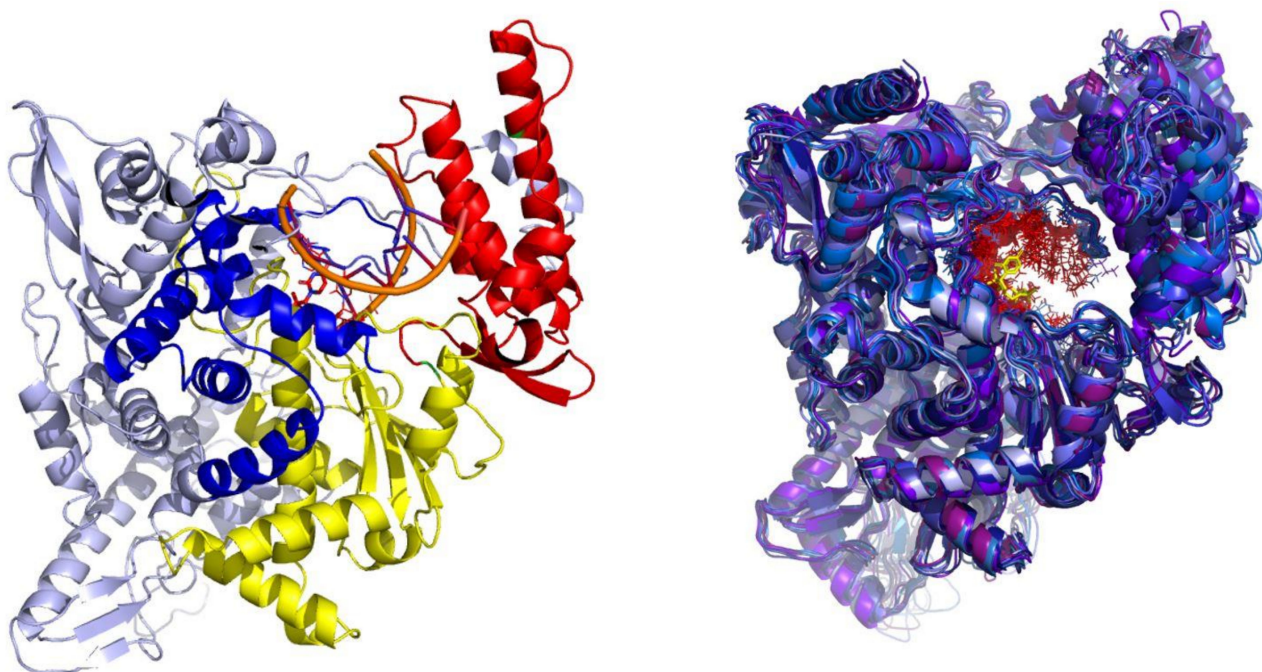


Figure 5. (Left) SARS-CoV-2 RdRp identified subdomains. Protein is presented in a cartoon model with the thumb subdomain in red, the palm subdomain in yellow and the fingers subdomain in blue. The RNA channel groove can be found in the central cavity between all three described subdomains (RNA in orange is superimposed from PDB ID: 4WTG for demonstration). (Right) Structural superimposition of the clustered centroids representing the conformational flexibility of the SARS-CoV-2 RdRp during the MD experiment. Centrally colored in red is the identified binding site with superimposed sofosbuvir from PDB ID: 4WTG in yellow.

The receptor structure was generated using the MakeReceptor GUI of OEDocking 3.2.0.2 software package (OpenEye Scientific Software, Inc., Santa Fe, NM, USA). A rectangular box with the volume of 9150 \AA^3 ($25.00 \text{ \AA} \times 18.33 \text{ \AA} \times 20.33 \text{ \AA}$) was defined around the sofosbuvir ligand superimposed in the previous step. A balanced site shape potential was calculated with docking volume of 1626 \AA^3 without applied central inner volume. No constraints were used, and active site residue conformations as well as protonation states were maintained.

5. Virtual Screening

The prepared 3D conformer library of 205 million structures was applied for HTVS with molecular docking into the pre-prepared RdRp receptor using FRED software from OpenEye (OpenEye Scientific Software, Inc., Santa Fe, NM, USA). In this protocol we employed normal-resolution docking parameters and Chemgauss4 scoring function [74–76]. HTVS was performed on an Intel® (Santa Clara, CA, USA) Xeon® E5-2630 v4 CPUs and 32 GB of memory machines using the Linux operating system. Statistical analysis of random compound samples (1000 samples taken from the pool of approximately 8 million docked compounds) revealed the docking scores reached a minimum of -13.234 and a maximum of 3.05 with a mean of -5.605 and a standard deviation of 1.233 . Normality was tested with a Shapiro–Wilk test using significance level of 0.05 . H_0 was not rejected (p value = 0.0536), and normality of FRED scoring values was assumed. Z-scores were therefore calculated for the whole docked library, and -5σ of top scoring compounds were selected for the final ensemble docking (3148 top-scoring compounds; docking score cut-off of -11.77) [77].

The RdRp docking ensemble was created from the clustered set of 20 protein conformations (obtained with ClusCo as already described before). Protein cluster alignment was checked with Theseus software that performed identically and confirmed the suitability of the clustering alignment [78]. Upon examination of each cluster size, 13 protein confor-

mations were selected for ensemble docking as they occupied more than 1% of the total trajectory time (cluster number–portion of the total trajectory time that the conformations of the relevant cluster occupy): 1–0.02, 2–0.04, 3–0.17, 4–0.02, 5–0.06, 6–0.12, 7–0.05, 8–0.19, 9–0.14, 10–0.08, 11–0.05, 12–0.03, 13–0.02. The following clusters were deemed not sufficiently influential for the ensemble docking as they occupied only a negligible portion of the total trajectory time: 14–0.006, 15–0.005, 16–0.004, 17–0.003, 18–0.001, 19–0.001, 20–0.001. Upon model selection, receptors were generated as already described before using MakeReceptor GUI of OEDocking 3.2.0.2 software package (OpenEye Scientific Software, Inc., Santa Fe, NM, USA) with default parameters (the box was resized to 21 Å in the x plane along the cavity surrounded by the palm and the finger subdomains). No constraints were used, and active site residue conformations as well as protonation states were maintained. The -5σ of top scoring compounds were finally re-docked to the 13 representative RdRp conformations using FRED from OpenEye software, and the final ensemble score was calculated by Equation (1).

$$S_{ensemble} = \sum_{N=1}^{13} S_i \cdot W_i \quad (1)$$

Equation (1): Ensemble docking score calculation where S_i represents individual FRED docking scores and W_i the corresponding ensemble weights, respectively. W_i possesses the following values from 1 to 13 individuals: 0.02, 0.04, 0.05, 0.17, 0.03, 0.02, 0.08, 0.06, 0.12, 0.05, 0.19, 0.02 and 0.14 as identified from the relative cluster probabilities (sizes).

The identified top 200 scoring hits were subjected to clustering analysis in order to obtain representative top-scoring scaffolds. MACCS fingerprints were calculated for all compounds and, after similarity matrix calculation, were binned into 20 representative clusters. The five top-scoring and clustered compounds are presented below in Table 1 (extended hitlist can be found in Supplementary Materials).

Table 1. The top five hits from the high-throughput virtual screening (HTVS) on the SARS-CoV-2 RdRp together with three nucleoside mimic RdRp inhibitors for comparison. The extended list is provided in Supplementary Materials.

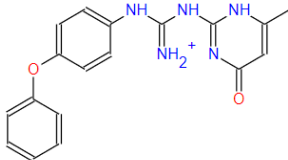
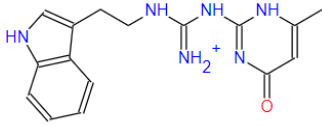
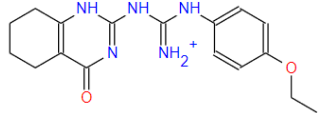
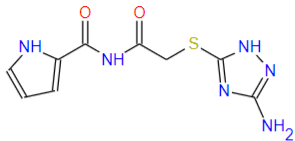
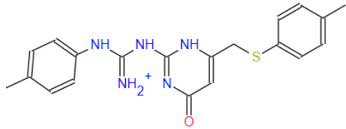
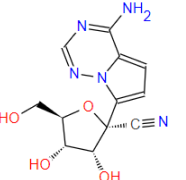
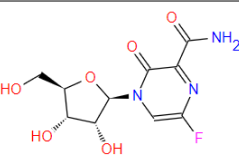
No.	Structure	Mr (g/mol)	Smiles	Cluster	Ensemble Docking Score
1		336.4	<chem>CC(NC(NC(Nc(cc1)ccc1O)c1ccccc1)=[NH2+])=N1=CC1=O</chem>	13	−12.72
2		311.4	<chem>CC(N=C(NC(NCCc1c[nH]c2c1ccccc2)=[NH2+])N1)=CC1=O</chem>	11	−12.68
3		328.4	<chem>CCOc(cc1)ccc1NC(NC(NC=C2CCCC1)=[NC2=O])=[NH2+]</chem>	15	−12.23
4		266.3	<chem>Nc1n[nH]c(SCC(NC(c2ccc[nH]2)=O)=O)n1</chem>	2	−11.59

Table 1. Cont.

No.	Structure	Mr (g/mol)	Smiles	Cluster	Ensemble Docking Score
5		380.5	<chem>Cc(cc1ccc1)NC(NC(NC(CSc1ccc(C)cc1)=C1)=NC1=O)=[NH2+]</chem>	14	−11.51
6*	 GS-441524 (remdesivir metabolite)	291.3	<chem>C1(C(N)=N2)N(N=C2)C(=CC=1)[C@@](O1)(C#N)[C@@H]([C@H](O)[C@H]1CO)O</chem> /	/	−10.96
7*	 favipiravir-ribose	289.2	<chem>[C@@H]1(N(C=C2F)C(=O)C(=N2)C(=O)N)O[C@H](CO)([C@@H](O)[C@H]1O)</chem> /	/	−10.78
8*	 GS-461203 (sofosbuvir metabolite)	260.2	<chem>C1=CC(NC(=O)N1[C@H](O[C@H]1CO)[C@](C)(F)[C@@H]1O)=O</chem> /	/	−10.24

* compounds docked as phosphates and depicted herein for comparison.

6. Free-Energy Calculations

From the top five scoring hits, compounds **1**, **2**, **3** and **5** constitute a similar structural class with a central guanidine linker, flanked by two aryl systems, while compound **4** displays a unique central thioether–amide linkage between terminal triazole and pyrrole heterocycles. All compounds also exhibit an analogous calculated binding mode as elaborated in Section 7. Therefore, compound **1** from the first structural class and compound **4** with FRED ensemble docking scores of −12.72 and −11.59, respectively, were selected for subsequent binding free energy calculations. Consequently, the Linear Interaction Energy (LIE) methodology developed by Aqvist et al. was employed [79]. It is especially suitable for ligand–receptor complex interaction studies and reported as superior to the MM/GBSA method commonly employed for this task [80]. To this end, we separately calculated the average VdW and electrostatic interaction energies of ligands **1** and **4** with water (explicit TIP3P solvent model) and of the ligands in complex with the solvated RdRp. Then, binding free energies of ligands **1** and **4** to RdRp were computed using Equation (2).

$$\Delta G_{LIE}^{bind} = \alpha \sum_i^N \Delta V_i^{vdW} + \beta \sum_i^N \Delta V_i^{coulomb} \quad (2)$$

Equation (2): The Δ term indicates the difference in average interaction energy between the ligand bound (in solvated RdRp) and ligand free (in water) states. The α and β represent LIE empirical parameters, determined by comparing calculated and experimentally measured binding affinities. Their values were optimized by Aqvist et al. [49].

For the LIE approach the MD simulations of 100 ns of clustered complexes from the ensemble docking (13 complexes for two ligands, 26 in total) as well as of free ligands in water were carried out to obtain the vdW and electrostatic interaction energies between the

ligands and their surroundings. Each MD simulation afforded 1000 snapshots (using 100 ps intervals) of each compound in protein bound and water environments for electrostatic and vdW interaction energy calculations. Interaction energies were averaged for the ligand free simulations (two sets separately for compounds **1** and **4**), while ligand bound potential energies were weighted according to Equation (3) and subsequently used in the LIE calculation [81–83].

$$W_i = \frac{e^{-\Delta G_{calc, i} / k_b T}}{\sum_i e^{-\Delta G_{calc, i} / k_b T}} \quad (3)$$

Equation (3): Weighting of ligand interaction energies as per Aqvist et al. (k_b -Boltzmann constant in J·K⁻¹).

Weighted LIE calculation (Table 2) resulted in the favorable affinity towards RdRp for compound **1** with ΔG_{LIE}^{bind} value of -2.6 ± 0.6 and for compound **4** with ΔG_{LIE}^{bind} value of -6.5 ± 0.8 kcal/mol using the preoptimized α and β parameters. Moreover, ligand–protein contact and RMSD analyses along all 13 MD production runs of compounds **1** and **4** confirmed a stable binding conformation and an analogous binding mode.

Table 2. Calculation of binding free energies for compounds **1** and **4** using the LIE methodology.

Compound	Free VdW (Kcal/Mol)	Free Coulomb (Kcal/Mol)	Complex VdW Weighted Sum (Kcal/Mol)	Complex Coulomb Weighted Sum (Kcal/Mol)	ΔG_{LIE}^{BIND} (Kcal/Mol)
1	-6.0 ± 0.1	-19.8 ± 0.2	-9.3 ± 0.5	-19.1 ± 0.6	-2.6 ± 0.6
4	-3.4 ± 0.1	-46.0 ± 0.8	-6.6 ± 0.1	-49.4 ± 0.8	-6.5 ± 0.8

7. Results and Discussion

After the SARS-CoV-2 RNA-dependent RNA polymerase (RdRp) active site identification based on subdomain locations, we postulated that the active site gorge is accessible and free to bind the nucleotides passing through the nucleotide channel. This hypothesis is corroborated by the cryoEM RdRp experimental structure (PDB ID: 6M71) by Gao et al. [42]. Moreover, the active site aspartate residues protruding from a *beta*-turn of the palm subdomain were identified at the RNA channel (PDB ID: 6M71 numbering: Asp760, Asp761), and the superimposition with HCV RdRp (PDB ID: 4WTG) placed its small-molecule inhibitor sofosbuvir (reference) at the active site analogously to the remdesivir binding pose postulated by Gao et al. [42].

All docked compounds were positioned at the bottom of the nucleotide binding gorge sandwiched between the key Asp623 and Asp760 residues. All top-scoring compounds displayed a similar binding motif; therefore, the best-scoring compound **1** from Table 1 will be discussed in more detail. Compound **1** forms hydrogen bonds of its central guanine linker with key Asp623, Lys621 and Arg553 as well as hydrophobic contacts with Arg553 and Lys621 (Figure 6). The central linker also forms a salt bridge with Asp623, while the compound **1** pyrimidine-4-one moiety is interacting with Arg555, but analogous binding modes of the remaining top-scoring compounds extend the terminal part of their molecules towards the Lys621 and Tyr455 pocket as well. All compounds make use of described distal pockets with their cyclic and/or aromatic moieties while placing their central linker or terminal moieties in the vicinity of the key Asp632 and Asp760 residues. Compounds also display a propensity to establish π – π interactions with Tyr455 or cat- π interactions with Lys621. An elegant direct ensemble docking–Linear Interaction Energy coupling methodology was employed to assess the binding propensity of the identified hit compounds as described beforehand [84]. All presented compounds are stably positioned near the postulated *remdesivir* binding pose, exhibit favorable ΔG_{LIE}^{bind} values and can effectively block the RNA matrix access to the RdRp catalytic pocket when bound in the predicted conformation.

We firmly believe that this work will facilitate further research into SARS-CoV-2 RdRp inhibitor design and provide the groundwork for the biological evaluation of innovative non-nucleoside RdRp inhibitors with the ultimate goal of effectively developing new probes for SARS-CoV-2 studies or novel drugs against COVID-19 and related viral diseases.

Supplementary Materials: The following are available online at <https://www.mdpi.com/article/10.3390/ijms222011143/s1>.

Author Contributions: Conceptualization, M.J., D.J. and U.B.; methodology, M.J., D.J. and U.B.; formal analysis, M.J., D.J. and U.B.; investigation, M.J., D.J. and U.B.; data curation, M.J., D.J. and U.B.; writing—original draft preparation, M.J., D.J. and U.B.; writing—review and editing, M.J., D.J. and U.B.; project administration, M.J., D.J. and U.B.; funding acquisition, D.J. and U.B. All authors have read and agreed to the published version of the manuscript.

Funding: This work was supported by the Slovenian Ministry of Science and Education through project grants OP20.04342 and HPC-RIVR as well as by the Slovenian Research Agency (ARRS) through program and project grants P2-0046, J1-1715, J1-9186, N1-0209 and J1-2471.

Institutional Review Board Statement: Not applicable.

Informed Consent Statement: Not applicable.

Data Availability Statement: The extended hitlist of compounds is available in the Supplementary Materials.

Acknowledgments: We gratefully acknowledge the support of NVIDIA Corporation with the donation of GPU hardware that was used in this research. We thank OpenEye for the academic licensing of their software and their help and support. We thank Elmar Krieger for his support and help.

Conflicts of Interest: The authors declare no conflict of interest.

Abbreviations

MD: molecular dynamics; RdRp: RNA-dependent RNA polymerase; VS: virtual screening; HTVS: high throughput virtual screening; HCV: Hepatitis C Virus; RMSD: root mean square deviation.

References

1. Gorbalenya, A.E.; Baker, S.C.; Baric, R.S.; de Groot, R.J.; Drosten, C.; Gulyaeva, A.A. Coronaviridae Study Group of the International Committee on Taxonomy of Viruses The Species Severe Acute Respiratory Syndrome-Related Coronavirus: Classifying 2019-NCoV and Naming It SARS-CoV-2. *Nat. Microbiol.* **2020**, *5*, 536–544. [[CrossRef](#)]
2. Zhu, N.; Zhang, D.; Wang, W.; Li, X.; Yang, B.; Song, J.; Zhao, X.; Huang, B.; Shi, W.; Lu, R.; et al. A Novel Coronavirus from Patients with Pneumonia in China, 2019. *N. Engl. J. Med.* **2020**, *382*, 727–733. [[CrossRef](#)] [[PubMed](#)]
3. Cui, J.; Li, F.; Shi, Z.-L. Origin and Evolution of Pathogenic Coronaviruses. *Nat. Rev. Microbiol.* **2019**, *17*, 181–192. [[CrossRef](#)]
4. de Wit, E.; van Doremalen, N.; Falzarano, D.; Munster, V.J. SARS and MERS: Recent Insights into Emerging Coronaviruses. *Nat. Rev. Microbiol.* **2016**, *14*, 523–534. [[CrossRef](#)] [[PubMed](#)]
5. Hilgenfeld, R.; Peiris, M. From SARS to MERS: 10 Years of Research on Highly Pathogenic Human Coronaviruses. *Antivir. Res.* **2013**, *100*, 286–295. [[CrossRef](#)]
6. Lu, G.; Wang, Q.; Gao, G.F. Bat-to-Human: Spike Features Determining ‘Host Jump’ of Coronaviruses SARS-CoV, MERS-CoV, and Beyond. *Trends Microbiol.* **2015**, *23*, 468–478. [[CrossRef](#)]
7. Wu, F.; Zhao, S.; Yu, B.; Chen, Y.-M.; Wang, W.; Song, Z.-G.; Hu, Y.; Tao, Z.-W.; Tian, J.-H.; Pei, Y.-Y.; et al. A New Coronavirus Associated with Human Respiratory Disease in China. *Nature* **2020**, *579*, 265–269. [[CrossRef](#)]
8. Li, Q.; Guan, X.; Wu, P.; Wang, X.; Zhou, L.; Tong, Y.; Ren, R.; Leung, K.S.M.; Lau, E.H.Y.; Wong, J.Y.; et al. Early Transmission Dynamics in Wuhan, China, of Novel Coronavirus-Infected Pneumonia. *N. Engl. J. Med.* **2020**, *382*, 1199–1207. [[CrossRef](#)]
9. Hui, D.S.; I Azhar, E.; Madani, T.A.; Ntoumi, F.; Kock, R.; Dar, O.; Ippolito, G.; Mchugh, T.D.; Memish, Z.A.; Drosten, C.; et al. The Continuing 2019-NCoV Epidemic Threat of Novel Coronaviruses to Global Health—The Latest 2019 Novel Coronavirus Outbreak in Wuhan, China. *Int. J. Infect. Dis.* **2020**, *91*, 264–266. [[CrossRef](#)]
10. Wang, C.; Horby, P.W.; Hayden, F.G.; Gao, G.F. A Novel Coronavirus Outbreak of Global Health Concern. *Lancet* **2020**, *395*, 470–473. [[CrossRef](#)]
11. Johns Hopkins University. Mortality Analyses. Available online: <https://coronavirus.jhu.edu/data/mortality> (accessed on 9 October 2021).

12. O'Driscoll, M.; Ribeiro Dos Santos, G.; Wang, L.; Cummings, D.A.T.; Azman, A.S.; Paireau, J.; Fontanet, A.; Cauchemez, S.; Salje, H. Age-Specific Mortality and Immunity Patterns of SARS-CoV-2. *Nature* **2021**, *590*, 140–145. [[CrossRef](#)]
13. Cortegiani, A.; Ingoglia, G.; Ippolito, M.; Giarratano, A.; Einav, S. A Systematic Review on the Efficacy and Safety of Chloroquine for the Treatment of COVID-19. *J. Crit. Care* **2020**, *57*, 279–283. [[CrossRef](#)]
14. Gao, J.; Tian, Z.; Yang, X. Breakthrough: Chloroquine phosphate has shown apparent efficacy in treatment of COVID-19 associated pneumonia in clinical studies. *Biosci. Trends* **2020**, *14*, 72–73. [[CrossRef](#)]
15. Yao, X.; Ye, F.; Zhang, M.; Cui, C.; Huang, B.; Niu, P.; Liu, X.; Zhao, L.; Dong, E.; Song, C.; et al. In Vitro Antiviral Activity and Projection of Optimized Dosing Design of Hydroxychloroquine for the Treatment of Severe Acute Respiratory Syndrome Coronavirus 2 (SARS-CoV-2). *Clin. Infect. Dis.* **2020**, *71*, 732–739. [[CrossRef](#)]
16. Gautret, P.; Lagier, J.-C.; Parola, P.; Hoang, V.T.; Meddeb, L.; Mailhe, M.; Doudier, B.; Courjon, J.; Giordanengo, V.; Vieira, V.E.; et al. Hydroxychloroquine and Azithromycin as a Treatment of COVID-19: Results of an Open-Label Non-Randomized Clinical Trial. *Int. J. Antimicrob. Agents* **2020**, *56*, 105949. [[CrossRef](#)] [[PubMed](#)]
17. Wang, M.; Cao, R.; Zhang, L.; Yang, X.; Liu, J.; Xu, M.; Shi, Z.; Hu, Z.; Zhong, W.; Xiao, G. Remdesivir and Chloroquine Effectively Inhibit the Recently Emerged Novel Coronavirus (2019-nCoV) In Vitro. *Cell Res.* **2020**, *30*, 269–271. [[CrossRef](#)] [[PubMed](#)]
18. Agostini, M.L.; Andres, E.L.; Sims, A.C.; Graham, R.L.; Sheahan, T.P.; Lu, X.; Smith, E.C.; Case, J.B.; Feng, J.Y.; Jordan, R.; et al. Coronavirus Susceptibility to the Antiviral Remdesivir (GS-5734) Is Mediated by the Viral Polymerase and the Proofreading Exoribonuclease. *mBio* **2018**, *9*, e00221-18. [[CrossRef](#)] [[PubMed](#)]
19. Ren, X.; Shao, X.X.; Li, X.X.; Jia, X.H.; Song, T.; Zhou, W.Y.; Wang, P.; Li, Y.; Wang, X.L.; Cui, Q.H. Identifying Potential Treatments Using a Data-Driven Approach. 2020. Available online: <https://blog.drugbankplus.com/data-driven-approaches-to-identify-potential-covid-19-therapies/?li=DB-home/Covid-1/1> (accessed on 9 October 2021).
20. Wu, Z.; McGoogan, J.M. Characteristics of and Important Lessons from the Coronavirus Disease 2019 (COVID-19) Outbreak in China: Summary of a Report of 72314 Cases from the Chinese Center for Disease Control and Prevention. *JAMA* **2020**, *323*, 1239. [[CrossRef](#)] [[PubMed](#)]
21. Li, G.; De Clercq, E. Therapeutic Options for the 2019 Novel Coronavirus (2019-nCoV). *Nat. Rev. Drug Discov.* **2020**, *19*, 149–150. [[CrossRef](#)]
22. Zhou, Y.; Hou, Y.; Shen, J.; Huang, Y.; Martin, W.; Cheng, F. Network-Based Drug Repurposing for Novel Coronavirus 2019-nCoV/SARS-CoV-2. *Cell Discov.* **2020**, *6*, 14. [[CrossRef](#)]
23. Jazzi, A.S.; Mahnam, K.; Hejazi, S.H.; Damavandi, M.S.; Sadeghi, P.; Zeinalian, M.; Khanahmad, H. Inhibition of Viral Macrodomein of COVID-19 and Human TRPM2 by losartan. *Preprints* **2020**, 2020030457. [[CrossRef](#)]
24. Dahly, D.; Gates, S.; Morris, T. Statistical review of hydroxychloroquine and azithromycin as a treatment of COVID-19: Results of an open-label nonrandomized clinical trial. *Zenodo* **2020**. [[CrossRef](#)]
25. Kolilekas, L.; Loverdos, K.; Giannakaki, S.; Vlassi, L.; Levounets, A.; Zervas, E.; Gaga, M. Can Steroids Reverse the Severe COVID-19 Induced “Cytokine Storm”? *J. Med. Virol.* **2020**, *92*, 2866–2869. [[CrossRef](#)] [[PubMed](#)]
26. Xu, X.; Han, M.; Li, T.; Sun, W.; Wang, D.; Fu, B.; Zhou, Y.; Zheng, X.; Yang, Y.; Li, X.; et al. Effective Treatment of Severe COVID-19 Patients with Tocilizumab. *Proc. Natl. Acad. Sci. USA* **2020**, *117*, 10970–10975. [[CrossRef](#)]
27. Favalli, E.G.; Ingegnoli, F.; De Lucia, O.; Cincinelli, G.; Cimaz, R.; Caporali, R. COVID-19 Infection and Rheumatoid Arthritis: Faraway, so Close! *Autoimmun. Rev.* **2020**, *19*, 102523. [[CrossRef](#)]
28. Misra, D.P.; Agarwal, V.; Gasparyan, A.Y.; Zimba, O. Rheumatologists' Perspective on Coronavirus Disease 19 (COVID-19) and Potential Therapeutic Targets. *Clin. Rheumatol.* **2020**, *39*, 2055–2062. [[CrossRef](#)]
29. Mehra, M.R.; Desai, S.S.; Ruschitzka, F.; Patel, A.N. RETRACTED: Hydroxychloroquine or Chloroquine with or without a Macrolide for Treatment of COVID-19: A Multinational Registry Analysis. *Lancet* **2020**, in press. [[CrossRef](#)]
30. Elfiky, A.A. Anti-HCV, Nucleotide Inhibitors, Repurposing against COVID-19. *Life Sci.* **2020**, *248*, 117477. [[CrossRef](#)]
31. Chang, Y.-C.; Tung, Y.-A.; Lee, K.-H.; Chen, T.-F.; Hsiao, Y.-C.; Chang, H.-C.; Hsieh, T.-T.; Su, C.-H.; Wang, S.-S.; Yu, J.-Y.; et al. Potential Therapeutic Agents for COVID-19 Based on the Analysis of Protease and RNA Polymerase Docking. Available online: <https://www.preprints.org/manuscript/202002.0242/v1> (accessed on 29 February 2020).
32. Imbert, I.; Guillemot, J.-C.; Bourhis, J.-M.; Bussetta, C.; Coutard, B.; Egloff, M.-P.; Ferron, F.; Gorbalenya, A.E.; Canard, B. A Second, Non-Canonical RNA-Dependent RNA Polymerase in SARS Coronavirus. *EMBO J.* **2006**, *25*, 4933–4942. [[CrossRef](#)]
33. Cheng, A.; Zhang, W.; Xie, Y.; Jiang, W.; Arnold, E.; Sarafianos, S.G.; Ding, J. Expression, Purification, and Characterization of SARS Coronavirus RNA Polymerase. *Virology* **2005**, *335*, 165–176. [[CrossRef](#)]
34. Romano, M.; Ruggiero, A.; Squeglia, F.; Maga, G.; Berisio, R. A Structural View of SARS-CoV-2 RNA Replication Machinery: RNA Synthesis, Proofreading and Final Capping. *Cells* **2020**, *9*, 1267. [[CrossRef](#)]
35. Lu, G.; Zhang, X.; Zheng, W.; Sun, J.; Hua, L.; Xu, L.; Chu, X.; Ding, S.; Xiong, W. Development of a Simple In Vitro Assay To Identify and Evaluate Nucleotide Analogs against SARS-CoV-2 RNA-Dependent RNA Polymerase. *Antimicrob. Agents Chemother.* **2020**, *65*, e01508-20. [[CrossRef](#)]
36. Wang, Y.; Anirudhan, V.; Du, R.; Cui, Q.; Rong, L. RNA-dependent RNA Polymerase of SARS-CoV-2 as a Therapeutic Target. *J. Med. Virol.* **2021**, *93*, 300–310. [[CrossRef](#)]
37. Elfiky, A.A. SARS-CoV-2 RNA Dependent RNA Polymerase (RdRp) Targeting: An in Silico Perspective. *J. Biomol. Struct. Dyn.* **2020**, *39*, 3204–3212. [[CrossRef](#)]

38. Kirchdoerfer, R.N.; Ward, A.B. Structure of the SARS-CoV Nsp12 Polymerase Bound to Nsp7 and Nsp8 Co-Factors. *Nat. Commun.* **2019**, *10*, 2342. [[CrossRef](#)]
39. Doublié, S.; Ellenberger, T. The Mechanism of Action of T7 DNA Polymerase. *Curr. Opin. Struct. Biol.* **1998**, *8*, 704–712. [[CrossRef](#)]
40. Elfiky, A.A.; Ismail, A.M. Molecular Docking Revealed the Binding of Nucleotide/Side Inhibitors to Zika Viral Polymerase Solved Structures. *SAR QSAR Environ. Res.* **2018**, *29*, 409–418. [[CrossRef](#)] [[PubMed](#)]
41. Larkin, M.A.; Blackshields, G.; Brown, N.P.; Chenna, R.; McGettigan, P.A.; McWilliam, H.; Valentin, F.; Wallace, I.M.; Wilm, A.; Lopez, R.; et al. Clustal W and Clustal X Version 2.0. *Bioinformatics* **2007**, *23*, 2947–2948. [[CrossRef](#)] [[PubMed](#)]
42. Gao, Y.; Yan, L.; Huang, Y.; Liu, F.; Zhao, Y.; Cao, L.; Wang, T.; Sun, Q.; Ming, Z.; Zhang, L.; et al. Structure of the RNA-Dependent RNA Polymerase from COVID-19 Virus. *Science* **2020**, *368*, 779–782. [[CrossRef](#)] [[PubMed](#)]
43. Kokic, G.; Hillen, H.S.; Tegunov, D.; Dienemann, C.; Seitz, F.; Schmitzova, J.; Farnung, L.; Siewert, A.; Höbartner, C.; Cramer, P. Mechanism of SARS-CoV-2 Polymerase Stalling by Remdesivir. *Nat. Commun.* **2021**, *12*, 279. [[CrossRef](#)]
44. Yin, W.; Mao, C.; Luan, X.; Shen, D.-D.; Shen, Q.; Su, H.; Wang, X.; Zhou, F.; Zhao, W.; Gao, M.; et al. Structural Basis for Inhibition of the RNA-Dependent RNA Polymerase from SARS-CoV-2 by Remdesivir. *Science* **2020**, *368*, 1499–1504. [[CrossRef](#)] [[PubMed](#)]
45. Elfiky, A.A. Novel Guanosine Derivatives as Anti-HCV NS5b Polymerase: A QSAR and Molecular Docking Study. *Med. Chem.* **2019**, *15*, 130–137. [[CrossRef](#)]
46. Elfiky, A.A.; Elshemey, W.M. Molecular Dynamics Simulation Revealed Binding of Nucleotide Inhibitors to ZIKV Polymerase over 444 Nanoseconds. *J. Med. Virol.* **2018**, *90*, 13–18. [[CrossRef](#)] [[PubMed](#)]
47. Elfiky, A.A.; Mahdy, S.M.; Elshemey, W.M. Quantitative Structure-Activity Relationship and Molecular Docking Revealed a Potency of Anti-Hepatitis C Virus Drugs against Human Corona Viruses. *J. Med. Virol.* **2017**, *89*, 1040–1047. [[CrossRef](#)]
48. Mastrangelo, E.; Pezzullo, M.; Tarantino, D.; Petazzi, R.; Germani, F.; Kramer, D.; Robel, I.; Rohayem, J.; Bolognesi, M.; Milani, M. Structure-Based Inhibition of Norovirus RNA-Dependent RNA Polymerases. *J. Mol. Biol.* **2012**, *419*, 198–210. [[CrossRef](#)] [[PubMed](#)]
49. Powdrill, M.H.; Bernatchez, J.A.; Götte, M. Inhibitors of the Hepatitis C Virus RNA-Dependent RNA Polymerase NS5B. *Viruses* **2010**, *2*, 2169–2195. [[CrossRef](#)]
50. Jácome, R.; Campillo-Balderas, J.A.; Ponce de León, S.; Becerra, A.; Lazcano, A. Sofosbuvir as a Potential Alternative to Treat the SARS-CoV-2 Epidemic. *Sci. Rep.* **2020**, *10*, 9294. [[CrossRef](#)]
51. Ruan, Z.; Liu, C.; Guo, Y.; He, Z.; Huang, X.; Jia, X.; Yang, T. SARS-CoV-2 and SARS-CoV: Virtual Screening of Potential Inhibitors Targeting RNA-dependent RNA Polymerase Activity (NSP12). *J. Med. Virol.* **2021**, *93*, 389–400. [[CrossRef](#)]
52. Beigel, J.H.; Tomashek, K.M.; Dodd, L.E.; Mehta, A.K.; Zingman, B.S.; Kalil, A.C.; Hohmann, E.; Chu, H.Y.; Luetkemeyer, A.; Kline, S.; et al. Remdesivir for the Treatment of Covid-19—Final Report. *N. Engl. J. Med.* **2020**, *383*, 1813–1826. [[CrossRef](#)]
53. Gordon, C.J.; Tchesnokov, E.P.; Feng, J.Y.; Porter, D.P.; Götte, M. The Antiviral Compound Remdesivir Potently Inhibits RNA-Dependent RNA Polymerase from Middle East Respiratory Syndrome Coronavirus. *J. Biol. Chem.* **2020**, *295*, 4773–4779. [[CrossRef](#)]
54. Lin, H.X.J.; Cho, S.; Meyyur Aravamudan, V.; Sanda, H.Y.; Palraj, R.; Molton, J.S.; Venkatachalam, I. Remdesivir in Coronavirus Disease 2019 (COVID-19) Treatment: A Review of Evidence. *Infection* **2021**, *49*, 401–410. [[CrossRef](#)] [[PubMed](#)]
55. Aftab, S.O.; Ghouri, M.Z.; Masood, M.U.; Haider, Z.; Khan, Z.; Ahmad, A.; Munawar, N. Analysis of SARS-CoV-2 RNA-Dependent RNA Polymerase as a Potential Therapeutic Drug Target Using a Computational Approach. *J. Transl. Med.* **2020**, *18*, 275. [[CrossRef](#)] [[PubMed](#)]
56. Shoichet, B.K. Interpreting Steep Dose-Response Curves in Early Inhibitor Discovery. *J. Med. Chem.* **2006**, *49*, 7274–7277. [[CrossRef](#)] [[PubMed](#)]
57. Baell, J.B.; Holloway, G.A. New Substructure Filters for Removal of Pan Assay Interference Compounds (PAINS) from Screening Libraries and for Their Exclusion in Bioassays. *J. Med. Chem.* **2010**, *53*, 2719–2740. [[CrossRef](#)] [[PubMed](#)]
58. Saubern, S.; Guha, R.; Baell, J.B. KNIME Workflow to Assess PAINS Filters in SMARTS Format. Comparison of RDKit and Indigo Cheminformatics Libraries. *Mol. Inf.* **2011**, *30*, 847–850. [[CrossRef](#)]
59. Harder, E.; Damm, W.; Maple, J.; Wu, C.; Reboul, M.; Xiang, J.Y.; Wang, L.; Lupyan, D.; Dahlgren, M.K.; Knight, J.L.; et al. OPLS3: A Force Field Providing Broad Coverage of Drug-like Small Molecules and Proteins. *J. Chem. Theory Comput.* **2016**, *12*, 281–296. [[CrossRef](#)]
60. Walters, W.P.; Stahl, M.T.; Murcko, M.A. Virtual Screening—An Overview. *Drug Discov. Today* **1998**, *3*, 160–178. [[CrossRef](#)]
61. Zhu, T.; Cao, S.; Su, P.-C.; Patel, R.; Shah, D.; Chokshi, H.B.; Szukala, R.; Johnson, M.E.; Hevener, K.E. Hit Identification and Optimization in Virtual Screening: Practical Recommendations Based on a Critical Literature Analysis: Miniperspective. *J. Med. Chem.* **2013**, *56*, 6560–6572. [[CrossRef](#)]
62. Sussman, J.L.; Lin, D.; Jiang, J.; Manning, N.O.; Prilusky, J.; Ritter, O.; Abola, E.E. Protein Data Bank (PDB): Database of Three-Dimensional Structural Information of Biological Macromolecules. *Acta Crystallogr. Sect. D Biol. Crystallogr.* **1998**, *54*, 1078–1084. [[CrossRef](#)]
63. Krieger, E.; Vriend, G. New Ways to Boost Molecular Dynamics Simulations. *J. Comput. Chem.* **2015**, *36*, 996–1007. [[CrossRef](#)]
64. Krieger, E.; Nielsen, J.E.; Spronk, C.A.E.M.; Vriend, G. Fast Empirical PKa Prediction by Ewald Summation. *J. Mol. Graph. Model.* **2006**, *25*, 481–486. [[CrossRef](#)] [[PubMed](#)]

65. Krieger, E.; Dunbrack, R.L.; Hooft, R.W.W.; Krieger, B. Assignment of Protonation States in Proteins and Ligands: Combining pKa Prediction with Hydrogen Bonding Network Optimization. In *Computational Drug Discovery and Design*; Baron, R., Ed.; Methods in Molecular Biology; Springer: New York, NY, USA, 2012; Volume 819, pp. 405–421, ISBN 978-1-61779-464-3.
66. Hornak, V.; Abel, R.; Okur, A.; Strockbine, B.; Roitberg, A.; Simmerling, C. Comparison of Multiple Amber Force Fields and Development of Improved Protein Backbone Parameters. *Proteins* **2006**, *65*, 712–725. [[CrossRef](#)]
67. Essmann, U.; Perera, L.; Berkowitz, M.L.; Darden, T.; Lee, H.; Pedersen, L.G. A Smooth Particle Mesh Ewald Method. *J. Chem. Phys.* **1995**, *103*, 8577–8593. [[CrossRef](#)]
68. Jamroz, M.; Kolinski, A. ClusCo: Clustering and Comparison of Protein Models. *BMC Bioinform.* **2013**, *14*, 62. [[CrossRef](#)]
69. Mulder, N.J.; Apweiler, R. The InterPro Database and Tools for Protein Domain Analysis. *Curr. Protoc. Bioinform.* **2003**, *2*, 2–7. [[CrossRef](#)]
70. McGuffin, L.J.; Bryson, K.; Jones, D.T. The PSIPRED Protein Structure Prediction Server. *Bioinformatics* **2000**, *16*, 404–405. [[CrossRef](#)]
71. Pearl, F.; Todd, A.; Sillitoe, I.; Dibley, M.; Redfern, O.; Lewis, T.; Akpor, A. The CATH Domain Structure Database and related resources Gene3D and DHS provide comprehensive domain family information for genome analysis. *Nucleic Acids Res.* **2004**, *33*, D247–D251. [[CrossRef](#)]
72. Appleby, T.C.; Perry, J.K.; Murakami, E.; Barauskas, O.; Feng, J.; Cho, A.; Fox, D.; Wetmore, D.R.; McGrath, M.E.; Ray, A.S.; et al. Structural Basis for RNA Replication by the Hepatitis C Virus Polymerase. *Science* **2015**, *347*, 771–775. [[CrossRef](#)]
73. Jácome, R.; Becerra, A.; Ponce de León, S.; Lazcano, A. Structural Analysis of Monomeric RNA-Dependent Polymerases: Evolutionary and Therapeutic Implications. *PLoS ONE* **2015**, *10*, e0139001. [[CrossRef](#)]
74. McGann, M. FRED and HYBRID Docking Performance on Standardized Datasets. *J. Comput. Aided Mol. Des.* **2012**, *26*, 897–906. [[CrossRef](#)] [[PubMed](#)]
75. McGann, M. FRED Pose Prediction and Virtual Screening Accuracy. *J. Chem. Inf. Model.* **2011**, *51*, 578–596. [[CrossRef](#)]
76. McGann, M.R.; Almond, H.R.; Nicholls, A.; Grant, J.A.; Brown, F.K. Gaussian Docking Functions. *Biopolymers* **2003**, *68*, 76–90. [[CrossRef](#)]
77. Amaro, R.E.; Baudry, J.; Chodera, J.; Demir, Ö.; McCammon, J.A.; Miao, Y.; Smith, J.C. Ensemble Docking in Drug Discovery. *Biophys. J.* **2018**, *114*, 2271–2278. [[CrossRef](#)]
78. Theobald, D.L.; Wuttke, D.S. THESEUS: Maximum Likelihood Superpositioning and Analysis of Macromolecular Structures. *Bioinformatics* **2006**, *22*, 2171–2172. [[CrossRef](#)]
79. Åqvist, J.; Medina, C.; Samuelsson, J.-E. A New Method for Predicting Binding Affinity in Computer-Aided Drug Design. *Protein Eng. Des. Sel.* **1994**, *7*, 385–391. [[CrossRef](#)]
80. Rifai, E.A.; van Dijk, M.; Vermeulen, N.P.E.; Yanuar, A.; Geerke, D.P. A Comparative Linear Interaction Energy and MM/PBSA Study on SIRT1–Ligand Binding Free Energy Calculation. *J. Chem. Inf. Model.* **2019**, *59*, 4018–4033. [[CrossRef](#)]
81. Hansson, T.; Marelis, J.; Åqvist, J. Ligand binding affinity prediction by linear interaction energy methods. *J. Comput. Aided Mol. Des.* **1998**, *12*, 27–35. [[CrossRef](#)]
82. Stjerschantz, E.; Oostenbrink, C. Improved Ligand-Protein Binding Affinity Predictions Using Multiple Binding Modes. *Biophys. J.* **2010**, *98*, 2682–2691. [[CrossRef](#)] [[PubMed](#)]
83. Klvana, M.; Bren, U. Aflatoxin B1–Formamidopyrimidine DNA Adducts: Relationships between Structures, Free Energies, and Melting Temperatures. *Molecules* **2019**, *24*, 150. [[CrossRef](#)] [[PubMed](#)]
84. Jukič, M.; Janežič, D.; Bren, U. Ensemble Docking Coupled to Linear Interaction Energy Calculations for Identification of Coronavirus Main Protease (3CLpro) Non-Covalent Small-Molecule Inhibitors. *Molecules* **2020**, *25*, 5808. [[CrossRef](#)] [[PubMed](#)]